Multistable grid and honeycomb shells

E. G. Loukaides[*], K. A. Seffen[†]

Department of Engineering, University of Cambridge, Trumpington Street, Cambridge CB2 1PZ, U.K.

13th December 2014

Abstract

The manufacturing of multistable shells has been dominated by the use of pre-stressed and composite materials. Here we advocate the use of common materials through a simple design that requires no pre-stressing and has an initially developable geometry. A rudimentary demonstrator is constructed and serves as the starting point for further study. An existing homogenisation model for a lattice structure is combined with an analytical strain energy model from the literature to show the mechanical properties needed to construct an initially developable, bistable grid shell. The concept is also tested in a commercial Finite Element package, where a number of parametric studies are performed. Both the demonstrator and the FE model confirm the validity of the design while a series of parametric studies helps establish the limits of this behaviour with respect to local and global geometry of grid shell and honeycomb structures.

Keywords: multistable, shell, grid, honeycomb, composite

1 Introduction

This work addresses the challenge of designing initially developable, <mark>free-standing</mark>, multistable shells without the use of composite materials or pre-stressing. Multistable shells have been

---

[*]Email: el249@cam.ac.uk
[†]Email: kas14@cam..ac.uk

the focus of much recent work since they offer a basis for the construction of morphing structures. They are able to support loads in distinct geometries, without the need for elaborate mechanisms. The manufacturing of multistable shells has been dominated by the use of pre-stressed materials and fibre-reinforced composites; in retrospect, this can be attributed to the work by Hyer (1981b), which introduced unsymmetric laminates as viable candidates for engineering applications of bistable shells. Laminates are attractive because they offer control of material properties through the orienting of the distinct laminae. However, laminates also have a number of disadvantages, namely, they are relatively expensive and they require skilled manual assembly and dedicated facilities. Perhaps most importantly, they are harder to employ in continuous large-scale (in the order of tens of metres and above) and small-scale (in the order of millimetres and below) structures.

At the same time, there has been a surge in the development of "smart materials," which often provide the basis for morphing structural applications. These can be expensive, offer highly specialised properties, and often are not straightforward to integrate within the host structure; hence, there is clear motivation to find alternative ways of controlling material properties. One attractive approach is to use the local geometry of a material; with such methods we can lower our dependence on more expensive and often harder-to-manufacture composite materials. Some ways of manipulating the macro-mechanical properties of shells through patterning and texturing have been studied previously in this context. Recent examples of such concepts exist in the form of corrugated shells (Norman *et al.*, 2008, 2009) and dimpled sheets (Golabchi & Guest, 2009).

Although these methods have their respective motivations and applications, here we seek as simple a technique as possible, to make manufacturing straightforward and scalable. Taking inspiration from earlier laminate designs, we note that the major stiffness contribution comes from the fibres; the matrix mostly serves as a binder for those more essential structural components. Similar properties can be obtained if we removed material from a solid plate of an isotropic material, in such a way that reproduces the stiffening action of the fibres along particular directions. The creation of perforations is both a simple procedure and an easily scalable one. This concept corresponds to grid shells,

honeycombs and perforated shells, whose global material properties can be manipulated by variations in the local geometry.

The theoretical treatment of multistable shells has most commonly employed the Uniform Curvature (UC) assumption, first used by Mansfield (1962). By considering "lenticular" sections, where the bending moment naturally diminishes at the periphery, he produced exact solutions of the Föppl-Von Kármán equations. The same author later justified the obvious weakness of the model to describe a known variation of the curvature at the boundary layer when constant thickness shells are considered. In Mansfield (2005), the approximate width of the boundary layer is calculated for an initially flat strip, thickness t, bent to a curvature κ along its length by end moments applied to its ends. The resulting width of $0.77\sqrt{t/\kappa}$ is very small for thin shells in large-deflection scenarios.

Hyer (1981a) produced an even simpler model, using the same UC assumption, and discretising the FVK equations with the Rayleigh-Ritz method. The simplicity of this model proved powerful in many instances and was used in various studies, especially relating to composite plates under thermal loads (Salamon & Masters, 1995; Dano & Hyer, 1998). At the same time, deficiencies of the UC assumption were noted, for example, Gigliotti *et al.* (2004) point out that the importance of planform aspect ratio is missed by both models. The failure of the UC assumption to exactly capture the boundary condition was mentioned above and led to various efforts to construct models with many more degrees of freedom (Aimmanee & Hyer, 2004; Pirrera *et al.*, 2011). This appears to be so when stretching effects dominate behaviour, for example, when the shell has initial Gaussian curvature. Coburn *et al.* (2013) show that the deformed shapes of spherical caps have boundary layers wider than Mansfield's approximation—because they possess significant Gaussian curvature, which can only be captured accurately using higher-order curvature distributions. Our initial and deformed shapes of shell are close to being developable throughout: stretching (and boundary layer) effects are minimal, which enables us to proceed with a uniform curvature assumption.

Bistable, developable shells are not new. In the context of MEMS, for example, we have various examples (Gerson *et al.*, 2012; Pham & Wang, 2011). These, however, contain

the well-known clamped, bistable arch and effectively rely on initially loaded boundaries for bistability to proceed. The shells presented here are unloaded and only restrained at one central point to prevent rigid body motion.

A set of workers persisted in extending the Mansfield model, especially in association with multistable shells, producing various practical results along the way. Guest & Pellegrino (2006) focused on a developable formulation that described bistable cylindrical shells, where bistability depends on the modular ratio between different orientations of the structure; Seffen (2007), accounting for both bending and stretching effects, showed that multistability is possible even for isotropic, pre-stressed shells; Vidoli & Maurini (2008) extended the scope of the examination by Seffen to describe the feasibility of a shallow, tristable, orthotropic shell; Fernandes *et al.* (2010), again with the same formulation, gave a method of quasi-statically actuating a bistable, pre-stressed shell. The analytical model used in the present work—an extension of the work in Seffen (2007)—clearly falls within this tradition, and the corresponding symbols are employed where appropriate.

The aim of the present study is to prove that grid shells and honeycomb shells can be made to be (at the very least) bistable when initially free of stresses and singly curved. Both types of shell are connected networks of beam-like elements, but their elastic responses differ because of relative differences in their local geometrical proportions. The cross-section of grid shell beams typically have comparable width and depth and thus, they respond locally as classical Euler-Bernoulli, or Timoshenko, beams. Honeycomb beams have a depth-to-width ratio greater than ten, and behave as slender webs, which are more prone to local distortions and instabilities when bending and torsion are locally applied; fundamentally, the Euler-Bernoulli hypothesis that cross-sectional shape remains conserved, is not guaranteed, and the beams have to be treated as plate-like elements aligned to the through-thickness direction (Cote *et al.*, 2004; Russell *et al.*, 2011). On the other hand, the elastic response of perforated plates, which are formed by drilling, or stamping out, holes in a thin homogenous plate, under simple in-plane loads can be found exactly by making use of the well-known solution for the stress-field around a hole (Slot & O'Donnell, 1971). This response is then cast as the set of effective orthotropic

4

properties, offered by an equivalent uniform plate without holes.

We address the feasibility of grid and honeycomb shells as bistable candidates by reversing the homogenisation process in the context of the previous well-known models of multistability: these models reveal the required range of effective orthotropic properties and initial uniform curvatures of the shell mid-surface. We assume from the outset that the effective properties of our shells do not depend on the initial uniform curvatures: so that homogenisation considers a flat shell, for simplicity and thus, we may decouple the realisation of the global geometry from the sizing of the local beam elements. The latter is aided by well-established homogenisation models for grid and honeycomb shells, which in their majority, however, only deal with in-plane loading. Converting these results into out-of-plane bending and twisting moduli for each type of shell usually follows the practice by which the so-called **ABD** matrices are obtained, by summing and integrating effects though the thickness (Mansfield, 2005). Here, this is appropriate when the local behaviour is beam-like, as in grid shells, because integration assumes implicitly that the cross-sectional shape is conserved. To our knowledge, this has not been tested for the deeper local beams in honeycomb shells, so we use the same process but treat the results with caution. In order to test and confirm our results, we resort to a complementary finite element analysis of both shells.

Section 2 presents a physical demonstrator constructed in the lab, which acts as motivation for the investigation that follows. Both grid shells and honeycomb shells can be defined by the same geometrical terms, which are introduced in Section 3. The overall geometry is dictated by the planform outline, its size and its initial curvature. Locally, the beam network is a symmetrical square mesh made up of interconnected prismatic sections governed by their length, width and height (or depth). Both sets of properties are hierarchically related in the relative senses of magnitude and orientation: the density of the grid network must be high enough for homogenisation to be effective in practical terms, and we describe the orientation by the angles between the local beam directions, the global axis of initial curvature and the global edges of shell. From the outset, we stipulate globally symmetrical layouts, in order to reduce the number of independent parameters,

and we focus on effective material properties for two such orientations. These are chosen to avoid anisotropic coupling for further simplicity, and the generalised Hooke's laws in extension and bending are expressed via the usual $\mathbf{A}$ and $\mathbf{D}$ matrices for orthotropic materials.

Using the earlier UC model (Section 4), we then show that multistability is concomitant to the effective torsional rigidity, α, and Poisson's ratio, ν, alone in the original dimensionless framework, with both taking values as large as possible. Their expressions are calculated from the Hooke's laws explicitly in terms of the ratios of the local geometrical parameters: we also calculate the stability landscape in terms of a range of values for each parameter, in order to identify the relative requirements between them for achieving bistability.

We then establish the set of geometrical parameters for our finite element "starting" model in Section 5, where we first focus on grid shells: we describe mesh generation, the choice of elements, the boundary conditions, solution control and how to establish multistable behaviour from the simulations. We also consider the sensitivity of performance to element density and we discuss the deviations in deformed equilibrium shape compared to the UC model assumptions. Parametric studies on bistability are then carried out by varying the initial radius of curvature and the height-to-width ratio of constituent beam elements. The latter frames further study on the effective depth of the grid shell, where deeper shells are considered to be honeycomb shells but which must be constituted of shell elements for accurate computational assessment. A parametric study follows, but not at the same level of detail as before for the sake of brevity. Out of interest, we show that a helically-curved honeycomb shell can also be bistable before concluding with a summary of our findings.

2 Physical demonstrator

The design and construction of a hand-held physical model was pursued, where the planform dimensions are in the order of decimetres. In terms of material, any isotropic material

satisfies the mechanical properties. However, the large deformations involved in travelling from one stable state to the next need to be considered. An intermediate flat state helps establish an upper ceiling for the required strains. For example, let us consider a cylindrical shell with a square $a \times a$ planform, a thickness h and initial curvature radius of curvature ρ_i. Considering a known symmetry for bistable cylindrical shells during the transition to a secondary state (Guest & Pellegrino, 2006), the originally curved direction of the shell ends up in an almost flat configuration. Hence an estimate for the strain upper limit of the extreme fibres is given by:

$$\epsilon = \frac{h}{2\rho_i} \tag{1}$$

For $h = 10\,\text{mm}$ and $\rho_i = 160\,\text{mm}$, values of practical concern here, $\epsilon \approx 3\%$, which is greater than typical maximum strains for metals; hence, we need to consider alternative materials. Thermoplastics fit the strain requirement; they can withstand strains above 10% before yielding, depending on the type of the plastic (Biron, 2012). In addition, they can be easily cut and drilled. Finally, they can be bent and shaped at a low temperature—the so-called crystalline melting point—below 200°C in some cases (Tripathi, 2002). If the material goes beyond this temperature, deforms and then cools to below its recrystallisation temperature, it retains its deformed shape.

A demonstrator is constructed out of a 6 mm sheet of the thermoplastic polypropylene (PP), which is cheap and widely available. A water-jet cutter is used to shape the desired local geometry, starting with a $300\,\text{mm} \times 300\,\text{mm}$ square. The side-length of unit cell—the "ligament" length, is 10 mm, and the target ligament thickness is 0.1 mm, which is very thin and leads to a few imperfections as seen in Fig. 1. The sample is then constrained by a cylindrical mould with a radius of 160 mm and heated to a temperature of 160°.

After cooling the sample to room temperature and removing the mould, we observe a spring-back effect—the demonstrator does not lose all residual stress during heating—but it remains cylindrically curved. There is also some local buckling of ligaments, since the sample was constrained to bend in the mould at room temperature. Nevertheless, bistable

behaviour is ascertained as documented in Fig. 2. The second state is almost cylindrical, with a smaller curvature orthogonal to the initial curvature but directed out-of-plane in the same sense, as predicted by both the simulations and the theoretical model; there is also a second, very mild principal curvature in the same direction. Repeated loading produces a relaxing effect, eventually taking the curvature outside the bistable region: but despite its lack of robustness, this novel structure proves the feasibility of almost developable multistable honeycombs.

3   Characteristics of grid shells and honeycombs

Grid shells—also known as lattice shells and reticulated shells—are defined globally in the same way as conventional shell structures but locally, we must account for their construction from beam-like elements rigidly connected to each other; this is carried out momentarily. There are numerous construction and cost benefits associated with grid shells, but here we note the following: they allow light through—at least much more so than a continuous structure; they allow the exchange of gases and fluids between the spaces that they define, which can be a critical characteristic in engineering applications; they are generally lighter than their continuous counterparts; and finally, in architectural terms, the particular discrete topology can be aesthetically desirable (Malek, 2012).

We now proceed to define a local geometry for the constituent beam-elements. We assume a rectangular cross-section for the members or ligaments and that all members are identical in dimensions: their exact dimensions are one subject of later analysis. Both the global pattern and the local geometry are displayed in Fig. 3, indicating a regular orthotropic grid and labelling of the beam-element geometry, specifically the length, height and width of the beam as d, h and b, respectively.

By considering different orientations for the grid shell, a dramatic variation of the in-plane mechanical properties can be achieved. For example, there must be a reduction in stiffness if we compare the effective Young's modulus in the X-direction vs that in the x-direction. In the former, deformation originates in the stretching of the beam-elements

while in the latter, their bending contributes the most. These effects are explained further in the next section.

For grid shells, it is reasonable to assume that members behave as beams provided the height-to-width ratio for the cross-section, h:b, remains small. Above a certain ratio, the structure becomes honeycomb-like, with deep members that must be treated as plate-like elements. The in-plane properties of grid-shells and honeycombs for a given pattern should be the same, but we expect the out-of-plane properties to vary significantly with the height of the elements, h. The distinction between them is quantified momentarily.

3.1 Homogenisation of mechanical properties

A square grid shell can easily allow adjustment of the modular ratio for an orthotropic shell by adjusting the cross-sectional areas of beam-elements in the two directions. At the same time, we can expect the Poisson's ratio to increase dramatically after the removal of material in such a pattern. An exaggerated effect can be visualised in the form of a square truss, with the nodes of the grid in our design corresponding to hinges in the truss and the strips of material corresponding to rod elements. Stresses in the diagonal direction clearly affect the geometry in the principal direction more intensely than on a solid plate. With this setup in mind, we can visualise the square pattern turning into a diamond-shaped pattern to accommodate the applied loading. The effect of loading along the principal direction would be carried by the structure along that same direction, with the perpendicular rods remaining unstressed, and hence with no geometrical change in that direction, *i.e.* the Poisson's ratio vanishes. In reality, there is some stiffness due to the nodes, and a truss equivalent is not ideal; it is more appropriate to consider each beam-element as having fixed supports at both ends, since symmetry dictates no rotation at the nodes. Consequently, the resulting displacements for a unit cell rotated by 45° and in tension are primarily due to the bending of the beam-elements. A diagram of expected deformation for a unit cell is shown in Fig. 3, overlaid on the original, unstressed square geometry.

For an elementary quantitative analysis, we turn to a model by Lebée & Sab (2013), which assumes the grid elements to be identical beams. While that work proceeds to describe a more elaborate, and more accurate formulation, we admit the simpler formulation for the purposes of this study. Here, the standard **ABD** notation for the constitutive properties of shells is used. The homogeneity of the grid shell in the out-of-plane z-direction ensures that the **B** matrix is zero. If we consider a square grid, as pictured in Fig. 3, then we have matrices **A** and **D** with respect to the local coordinate system (1-2-3), where 3 is the out-of-plane direction, given by:

$$\mathbf{A} = \begin{pmatrix} \dfrac{ES_1}{d} & 0 & 0 \\ 0 & \dfrac{ES_1}{d} & 0 \\ 0 & 0 & \left(\dfrac{d}{GS_2} + \dfrac{d^3}{12EI_3} \right)^{-1} \end{pmatrix}, \quad \mathbf{D} = \begin{pmatrix} \dfrac{EI_2}{d} & 0 & 0 \\ 0 & \dfrac{EI_2}{d} & 0 \\ 0 & 0 & \dfrac{GJ}{d} \end{pmatrix}, \tag{2}$$

where S_1 is the cross-sectional area of a beam ($= bh$) and S_2 is its shear area ($= hd$); I_2 and I_3 are moments of inertia about the 2 and 3 axes, respectively; E and G are moduli of the homogeneous material; and J is the torsion constant. An approximation for the latter for a rectangular section is found in Young & Budynas (2002), to be equal to:

$$J = hb^3 \left[\frac{1}{3} - 0.21 \frac{b}{h} \left(1 - \frac{b^4}{12h^4} \right) \right], \tag{3}$$

when $h > b$. The formulation for **D** again assumes beam-like behaviour for each element, with a neutral mid-surface of zero in-plane strains.

The **A** and **D** matrices noted above can be used to obtain the corresponding matrices in different orientations with a rotational transformation. For example, if we want to obtain equivalent in-plane, homogenised moduli for a sheet in a direction 45° to the direction of the beam-elements, we first apply a rotational transformation to **A**, producing:

$$\mathbf{A}_{\mathrm{d}} = \mathbf{A}_{45^\circ} = \begin{pmatrix} \dfrac{Ehb\left[d^3 + 2db^2 + 2b^3(1+\nu)\right]}{2d\left[d^3 + 2b^3(1+\nu)\right]} & \dfrac{Ehb\left[d^3 - 2db^2 + 2b^3(1+\nu)\right]}{2d\left[d^3 + 2b^3(1+\nu)\right]} & 0 \\ \dfrac{Ehb\left[d^3 - 2db^2 + 2b^3(1+\nu)\right]}{2d\left[d^3 + 2b^3(1+\nu)\right]} & \dfrac{Ehb\left[d^3 + 2db^2 + 2b^3(1+\nu)\right]}{2d\left[d^3 + 2b^3(1+\nu)\right]} & 0 \\ 0 & 0 & \dfrac{Ehb}{2d} \end{pmatrix},$$

$$(4)$$

where the d subscript refers to the diagonal (45°) orientation with respect to the unit cell's local geometry. From this, we can extract corresponding homogenised parameters quite easily:

$$\nu_{\mathrm{A}} = \frac{A_{\mathrm{d21}}}{A_{\mathrm{d11}}} = \frac{d^3 - 2db^2 + 2b^3(1+\nu)}{d^3 + 2db^2 + 2b^3(1+\nu)} \tag{5}$$

and

$$\alpha_{\mathrm{A}} = \frac{A_{\mathrm{d33}}}{A_{\mathrm{d11}}} = \frac{d^3 + 2b^3(1+\nu)}{d^3 + 2db^2 + 2b^3(1+\nu)}. \tag{6}$$

The same procedure can produce corresponding parameters for bending by operating on the $\mathbf{D}$ matrix. These are:

$$\nu_{\mathrm{D}} = \frac{A_{\mathrm{d21}}}{D_{\mathrm{d11}}} = \frac{-400h^5b^2 + 252h^4b^3 - 21b^7 + 100h^7(1+\nu)}{400h^5b^2 - 252h^4b^3 + 21b^7 + 100h^7(1+\nu)}, \tag{7}$$

and

$$\alpha_{\mathrm{D}} = \frac{D_{\mathrm{d33}}}{D_{\mathrm{d11}}} = \frac{100h^7(1+\nu)}{400h^5b^2 - 252h^4b^3 + 21b^7 + 100h^7(1+\nu)}. \tag{8}$$

We plot values of these parameters for different local dimensions in Fig. 4. The values for the Poisson's ratio and the shear modulus parameter, α, that correspond to the matrix $\mathbf{A}$ are almost unchanged by the variation of the geometry, where their values are very close to unity for the entire range of geometry that we are examining. The same values, when estimated from the corresponding $\mathbf{D}$ matrix vary significantly—in the range of 0 to 1 for ν and 0.5 to 1 for α. Recall that for our model to be valid $h > b$, hence we only plot the estimates for $h/b > 1$.

The homogenisation method becomes more accurate when the local dimensions are

much smaller than the planform dimensions of the shell. However, in the simulations that follow, we also have to balance that theoretical requirement with practical considerations, such as the constructibility of the shell and computational cost: we therefore choose the global dimensions to be more than 25 times the width of the unit cell and we note that we are dealing with elastic phenomena locally, where the properties reliably scale.

4   Analytical model

An expression for the strain energy stored in the deformed shell with components due to shallow bending and in-plane stretching is taken from Seffen & Maurini (2013) and is, in turn, an extension of previous work found in Seffen (2007) and Fernandes *et al.* (2010). We reproduce it here in its simplest dimensionless form, in the absence of pre-stressing and for an initially cylindrical configuration:

$$U = \left(\kappa_x \kappa_y - \kappa_{xy}^2 \right)^2 + \left[(\kappa_x - \kappa_{x0})^2 + 2\nu_D(\kappa_x - \kappa_{x0})\kappa_y + \kappa_y^2 + \alpha \kappa_{xy}^2 \right], \qquad (9)$$

κ_x and κ_y are the dimensionless observed curvatures, κ_{x0} is the dimensionless initial curvature of the shell, which is arbitrarily assigned to the x direction, ν_D is the out-of-plane Poisson's ratio and α is proportional to the in-plane shear modulus of the shell, and thus to α_D from the previous section. Also recall the α_A and ν_A parameters from the previous section which would normally be used to solve the membranal problem. In Seffen & Maurini (2013) the curvatures are made dimensionless by multiplying by the factor a^2/t, where a is the planform dimension for the shell and t is the thickness. Equilibrium states are given by minimising the energy stored according to calculus of variations; since our model exhibits no twisting curvature as observed in our demonstrator, we may assume solutions where $\kappa_{xy} = 0$ is valid. It can then be shown after differentiating U that the remaining non-zero curvatures are found by solving the coupled algebraic equations:

$$\kappa_x - \kappa_{x0} + \kappa_y(\kappa_x \kappa_y + \nu_D) = 0, \qquad \kappa_y - \kappa_{x0}\nu_D + \kappa_x(\kappa_x \kappa_y + \nu_D) = 0, \qquad (10)$$

Closed-form solutions are achievable, but too lengthy to be immediately useful, or presentable here; but it is clear from inspecting them that they are a function of the initial curvature and the Poisson's ratio only. The stability of solutions is then assessed by the Hessian of the same energy expression, specifically, for stability to be guaranteed, it is sufficient to show that all eigenvalues of the Hessian are positive for the equilibrium under consideration. The general form of the eigenvalues, λ, can be found as:

$$\lambda_1 = \alpha - 2\kappa_x\kappa_y, \qquad \lambda_{2,3} = \frac{1}{2}\left(2 + \kappa_x^2 + \kappa_y^2 \pm \sqrt{\kappa_x^4 + 14\kappa_x^2\kappa_y^2 + \kappa_y^4 + 16\kappa_x\kappa_y\nu_D + 4\nu_D^2}\right).$$

$$(11)$$

In λ_1, α does not cause instability for developable equilibria, but a minimum shear modulus is required for doubly curved equilibria to be stable. The second eigenvalue, λ_2, with a positive sign before the root, is always positive. The sign of the third eigenvalue depends on the relative magnitudes of κ_x, κ_y and ν. A brief numerical investigation proves the feasibility of bistability for such a structure, for a range of Poisson's ratio and shear modulus values, where the relevant plot is given in Section 5.2.1—with consideration for both in-plane and out-of-plane properties.

5 Finite-Element Analysis

This concept for a bistable shell is tested through Finite Element (FE) simulations on the commercial software package ABAQUS (Abaqus, Inc., 2007). A number of parameters are required to fully define the geometry of such a structure. In this section we assume an initial cylindrical geometry for a shell with a rectangular planform. Double curvature facilitates multistability—i.e. isotropic materials can be used for constructing doubly curved, bistable shells—so omitting it here ensures that the effects we observe are the product of global material properties, and not only of extensional effects. The set of required dimensions to fully define each geometry is as follows:

- Global geometry:

    - length of shell projection along x-direction (a_x)

13

- shell length along y-direction (a_y)

- cylinder radius of curvature—along x-direction(ρ_x)

- global thickness. The global thickness for a grid shell is not a directly accessible quantity. We can simply assume the value given to the local beam-member height, or we can treat it with various homogenisation methods.

- Local geometry (defined previously):

  - length of beam-members (d)

  - beam-member cross-section width (b)

  - beam-member cross-section height (h). We treat this as the global shell thickness as mentioned above.

These are shown in detail in Figs. 3 and 5.

ABAQUS has a graphical interface that facilitates defining the geometry of the structure we are examining, the loads, the boundary conditions etc. However, the resulting structures cannot be modified easily. In addition, the mesh-like, curved structure at the basis of our study, cannot be drawn with any standard tools and attempting to draw it manually (node by node) would be impractical. An alternative exists for the user in the direct use of input (`.INP`) files that ABAQUS can read in simple text and which define the entire simulation with appropriate commands. The writing of a text file can be easily automated and, in this case, the `.INP` file is written in the open source software language, PYTHON, as an executable script. In this script, the 3D coordinates of each node and member are defined in a parametric mathematical form, so that the local and global geometry can be changed by adjusting only the dimension(s) of interest—greatly assisting parametric studies. Similarly, all remaining options for the simulation are input as text commands.

The simulation is composed of two Dynamic Implicit steps, with quasi-static application—a method suitable for non-linear structural problems (Dassault Systémes/Simulia, 2011). The node corresponding to the centre of the shell is held fixed for all degrees of freedom.

In the first step we use displacement control on two nodes on opposite sides of the shell as shown in Fig. 6: all other nodes are unconstrained, allowing for the possibility of, for example, twisted shapes as well as ordinary curved deformations. During the second step, displacement control is removed and the shell is allowed to return to a load-free equilibrium geometry. Elements of type B31, a three-node linear beam element, are used with four elements per ligament after a brief mesh sensitivity study, see Fig. 7.

For a set of cases that follow, the global geometry is fixed and the effects of local geometry variations are examined. The global dimensions are fixed as follows: $a_x = 520\,\text{mm}$, $a_y = 520\,\text{mm}$, $\rho_x = 300\,\text{mm}$, thus mirroring a realistic design for a hand-held demonstrator. Later, the effect of the global curvature on multistability is also examined.

5.1   Proof of concept

We begin with one case in detail, to establish that bistability is feasible under these specifications. We fix the remaining spatial variables such that $d = 10\,\text{mm}$, $b = 0.2\,\text{mm}$, $h = 0.8\,\text{mm}$. For this ligament length the total number of elements is equal to 5184. The ratio of the length of the beam-member to the beam cross-sectional dimensions is greater than 100 and large enough for an Euler-beam assumption to be reasonable. The corner node is displaced by 150 mm along the z-axis over the duration of the first step, and both the loading and the relaxation steps have a duration of 100 s. The Young's Modulus for the material is set to equal those of aluminium at 69 GPa and the Poisson's ratio at 0.32, to reflect a realistic material. The corresponding homogenised material properties can be found through Eqs. (5) to (8) which give ν_A and α_A approximately equal to unity (0.998 and 0.999 respectively), and $\nu_\text{D} = 0.72$ and $\alpha_\text{D} = 0.86$.

We present a plot of the total strain energy in Fig. 8. During the loading period we see a clear minimum; when we remove the displacement boundary condition at the corner node, the strain energy settles at this value and does not return to an unstressed state. Both these observations confirm the existence of a second stable geometry for this shell. The initial state, as noted above, is perfectly cylindrical. The second state, on first

inspection, appears to be approximately cylindrical in the same sense as the initial state, but with the two directions of curvature reversed.

A detailed examination of the secondary stable geometry is shown in Fig. 9. The profiles of the shell in the x- and y-directions are isolated and plotted in two separate sets of axes. The first profile, in the direction of initial zero curvature (y), appears almost uniformly curved, with a larger radius of curvature than the initial state. A dotted, circular arc is also plotted in the same set of axes for visual comparison, and we observe an almost perfect match. The profile in the x-direction is drawn exaggerated in the z-direction. Although, the deviation from a flat profile is small, it is noticeable where, towards the centre, the shell is concave upwards. At an approximate radial distance of two thirds of the total shell radius, the curvature changes sign and is maintained until a boundary layer where the curvature is more pronounced. The deviation from the central node in the perpendicular direction does not exceed $13\,\mathrm{mm}$ at any point (less than 4.3% of the shell's half-width), while the maximum value is observed at the periphery. Given these results, it is appropriate to refer to the second stable configuration as almost cylindrical. Coburn *et al.* (2013) obtained similar results when producing, through composites, a tristable shell. This variation of curvatures was predicted in Vidoli (2013) using a coarse von Kármán model with quadratically varying curvature.

5.2 Parametric studies

To the authors' knowledge, this is the first time a grid shell has been investigated in the context of multistability. Hence, almost every parameter that we have treated as a constant in the basic case is worthy of further investigation, including local and global dimensions and their relative magnitudes. In this section, we limit our investigation to those parameters that appear the most critical or to the local geometry parameters that are not directly assessed by our UC model, namely the cross-sectional dimensions of the beam-elements. Later, the initial curvature and the moment of inertia of the beam-element are also investigated with respect to multistability.

5.2.1 Ligament height-to-width ratio

We focus first on the influence of the cross-sectional height of the member beams (h) on bistability. We fix all parameters except h and perform a series of simulations as described in Section 5. The cross-sectional width is set at $0.2\,\text{mm}$. The height is varied between that same value and increased by $0.2\,\text{mm}$ up to a value of $1.2\,\text{mm}$.

Results of this study are shown in Fig. 10, in the form of force-displacement diagrams. The value for the force is specific to the node also used for displacement control and shown in Fig. 6, while displacement, w, also refers to the same node. Both the force and displacement outputs are rendered dimensionless: the force is multiplied by $\rho_x/(Eh^3)$ and the displacement is divided by the apex height, H, shown in Fig. 5.

The resulting force-displacement graphs show a characteristic snap-through effect for all cases. As h is increased, the plot crosses the displacement axis for the first time when $h = 0.8\,\text{mm}$. The case of $h = 0.6\,\text{mm}$ is almost tangential to the displacement axis at its lowest point. Thus in this scenario, a ratio of $h{:}b$ greater than an approximate value of three is needed for bistability, while additional simulations for $h > 0.8\,\text{mm}$ are consistent.

We add to these conclusions by returning to the material properties for the grid shell obtained in Section 3.1 in Fig. 11. We produce a colourmap of the stability regimes for specific global dimensions, matching the dimensions of the simulations, while varying the cross-sectional height and width, h and b respectively. This plot supports a constant minimum ratio of $h{:}b$ for bistability to be possible, with a value close to five. Recall from earlier in this section that this is in rough agreement with our simulations, which show an approximate value slightly above three for a similar scenario.

For larger $h{:}b$ ratios our beam assumption becomes defunct. Once h and d have comparable values, and while b retains a small relative value ($20b < h \approx d$), it is reasonable to begin treating each ligament as a plate element. This results in a global honeycomb structure and is investigated further in Section 5.3. We should note that repetition of this study with a change in cross-sectional width shows that the ratio of the two cross-sectional dimensions is the critical parameter and not the absolute value of one or the other.

5.2.2 Initial curvature

Another critical parameter for bistability, is the initial curvature of the shell, with respect to a planform of constant dimensions. Equivalently, we may consider the apex height of the shell as the critical parameter, since the three parameters are related, with the global geometry from Fig. 5. The relevant series of FE simulations fixes the planform dimensions, a_x and a_y, as all other simulations to be square: $520\,\text{mm} \times 520\,\text{mm}$. The ligament cross-section is $0.1\,\text{mm} \times 0.4\,\text{mm}$, the length of the ligaments is $10\,\text{mm}$ and the initial radius of curvature, ρ_x, varies between $300\,\text{mm}$ and $550\,\text{mm}$ at $50\,\text{mm}$ intervals.

The results of the parametric study are shown in Fig. 12, where dimensionless force-displacement diagrams are plotted for all the tested values. The last case to be marginally bistable, for increasing values of the curvature, corresponds to a global radius of curvature equal to $450\,\text{mm}$, with a depth-to-planform length ratio equal to 0.16. Although this is a specific case with absolute dimensions, the trend observed can greatly inform future physical designs.

5.2.3 Cross-sectional scaling

A notable observation regarding the strain energy of the shell is obtained by scaling the dimensions of the cross-section: the ratio $h{:}b$ is kept fixed (at a value of three) with the absolute values of the (h, b) pair as $(0.02\,\text{mm}, 0.06\,\text{mm})$, $(0.1\,\text{mm}, 0.3\,\text{mm})$ and $(0.2\,\text{mm}, 0.6\,\text{mm})$. The strain energy from the simulations is pre-multiplied by a factor hb^3 and is plotted in Fig. 13, where all curves match almost exactly. The scaling used matches the moment of inertia of the cross-section, which takes the form $hb^3/12$ for a rectangular cross-section; and a linear relationship between the strain energy and the local moment of inertia indicates bending-dominated behaviour throughout the geometrical transition.

5.3 Honeycombs

Honeycombs are a natural extension of grid shells. We make the distinction between the two to mainly signify a change in our assumptions about the relative ratios of the

parameters h, b and d. We use the same square pattern as for grid shells, and we use the same symbols for the geometry as before

A series of FE simulations are performed under the plate assumption for the ligament geometry. The model has the same global parameters as the earlier grid shell model: locally, the distance between nodes, or the ligament length (d) is initially set at 10 mm, while the ligament thickness is fixed at 0.1 mm. The ratio of $d{:}b$ is large enough to admit a plate geometry, as long as the h parameter is also sufficiently large. We only admit h values greater than 2 mm, or a ratio of $h{:}b$ greater than 20.

The ABAQUS model extends the grid shell model using an additional layer of nodes, which is added at a radial offset from the original set. All nodes now define the corners of the connecting ligaments shell-elements, whose middle surface is orthogonal to the global shell's middle surface. Four-noded quadrilateral S4R shell elements are chosen to maintain a reasonably fast simulation, where the number of elements is fixed at 4×4 per rectangular plate-ligament. With $d = 10$ mm and planform dimensions 520 mm $\times$ 520 mm, a total of approximately 80000 elements are needed.

One immediate goal is to establish the limit of bistable behaviour with respect to large values of h. In Fig. 14 we plot the strain energy for various values of h where only the early part containing possible strain energy minima is required. For low values of h, the plots are consistent with the grid shell simulations and a clear minimum for the strain energy appears during the loading phase. This minimum is eventually lost for values of $h = 30$ mm and higher. A value of $h = 25$ mm also allows bistability, but is omitted from the plot for clarity.

In Fig. 15 snapshots from one simulation are displayed for two reasons: they help visualise the differences in local geometry of the honeycomb model with the earlier grid shell model, and they give a clear image of the intermediate and final stable equilibria of the honeycomb shell. With respect to the latter, the secondary stable configuration is extremely similar to the one obtained for grid shells, during the transition however, the honeycomb forms a saddle-shape, a behaviour that is not observed for grid shells to such an extent.

A stability overview of the corresponding homogeneous shell with the same global dimensions is also offered in Fig. 16 with respect to the shear modulus, G, and the thickness of the shell, t. The material properties are arbitrarily chosen to roughly correspond to the analysis in Section 3.1; the Poisson's ratio is set at 0.95—a high value that fits the theoretical requirement—and orthotropic behaviour is assumed. Figure 16 shows that we cannot obtain bistability for a narrow band of low shear modulus, when G/G_{iso} is less than two. When the shear modulus is sufficiently large for bistable behaviour, bistability is lost at an approximate thickness of $22\,\mathrm{mm}$, which increases marginally with the value of the shear modulus. The theoretical result is in rough agreement with the results of the FE simulations.

The comparison with theory is expanded in Fig. 17, which shows first in Fig. 17a contours of the strain energy across the (κ_x, κ_y) plane for a thickness of $10\,\mathrm{mm}$. There are two distinct minima corresponding to two cylindrical geometries, and the curvature of the second state is slightly smaller. After connecting the two minima with a straight line, the strain energy is plotted along this profile. This sectioning allows for the theoretical result corresponding to Fig. 14 to be plotted in Fig. 17b. The deformation path during actuation is not explicitly plotted here, but can be extrapolated from Fig. 17a and is consistent with the hyperbola $\kappa_x \kappa_y = $ constant, i.e. the shell proves to be almost inextensible. The loss of the second energy minimum is the focus here, and for this purpose this profile suffices. A rough agreement with the FE simulations is again immediate.

5.4 Helical grid shell

The geometrical possibilities for a bistable grid shell are not limited to neither shallow shells nor square planforms. In order to test matters, we arbitrarily chose a helicoidal shell with dimensions similar to earlier structures. The ABAQUS planform is a rhomboid with sides of $300\,\mathrm{mm}$ and $900\,\mathrm{mm}$ with its largest internal angle equal to $\left(\frac{\pi}{2} + \arctan\frac{1}{2}\right)$. The shortest side is parallel to the x-direction, and the rhomboid is then wrapped along a cylindrical mathematical surface with its axis parallel to the x-direction. The initial

geometry is displayed in Fig. 18a, where the cross-section of the ligaments is once again assumed to be rectangular with dimensions $0.2\,\text{mm} \times 0.8\,\text{mm}$. The shell is loaded by displacement control of the centre nodes on the two shorter sides, which are displaced along the y-direction, beyond the flattening of the grid shell in this direction, and then released. A two step, Dynamic Implicit model is setup in ABAQUS, as with earlier simulations. The strain energy of the system is shown in Fig. 18b.

A clear minimum is seen after a sudden dip during the loading phase (0–100 s). After the relaxation phase, the strain energy returns to the geometry of a secondary geometry, in agreement with the earlier minimum value. The secondary stable geometry is also shown in Fig. 18a and closely matches a cylindrical surface, with an axis along the y-direction. Such a design potentially allows for more control of the stiffness in both directions contrary to the shallower, square design.

6   Summary and concluding remarks

This work has investigated a novel multistable shell without using composite or prestressed materials. By taking advantage of the change in global material properties from the patterning of grid shells and honeycomb shells, suitable designs can produce multistability in relatively simple structures. In contrast to composite designs, this method is easily scalable—from the micro to the architectural scale. In addition, it facilitates light and fluid permeable structures. The construction of a thermoplastic demonstrator honeycomb confirmed the bistable nature of such a structure, albeit short-lived due to creep effects; there is considerable scope for an improved model. A series of FE simulations helped us understand the necessary local patterning with respect to the global dimensions. Specifically, developable shells were investigated. Parametric studies focused on the limits of multistability with respect to the global thickness of the shells and to the global radius of curvature. In addition the predicted initial and secondary global geometry for bistable grid shells were explored. Finally, the FE simulations indicated that the deformation is bending dominated.

This study is not exhaustive but it establishes the feasibility of multistability in the context of grid shells and honeycomb shells. This discovery invites further examination of our assumptions for material homogenisation and motivates the investigation of more elaborate patterns—potentially to increase the energy barrier between stable states and to address boundary effects. We look forward to pursuing such work in the future.

Acknowledgments

References

ABAQUS, INC. (2007). *Abaqus/CAE user's manual*.

AIMMANEE, S. & HYER, M.W. (2004). Analysis of the manufactured shape of rectangular thunder-type actuators. *Smart Materials and Structures*, **13**, 1389.

BIRON, M. (2012). *Thermoplastics and Thermoplastic Composites*. Elsevier.

COBURN, B.H., PIRRERA, A., WEAVER, P.M. & VIDOLI, S. (2013). Tristability of an orthotropic doubly curved shell. *Composite Structures*, **96**, 446–454.

COTE, F., DESHPANDE, V., FLECK, N. & EVANS, A. (2004). The out-of-plane compressive behavior of metallic honeycombs. *Materials Science and Engineering: A*, **380**, 272–280.

DANO, M.L. & HYER, M.W. (1998). Thermally-induced deformation behavior of unsymmetric laminates. *International Journal of Solids and Structures*, **35**, 2101–2120.

DASSAULT SYSTÉMES/SIMULIA (2011). *Getting started with Abaqus v6.11*.

Fernandes, A., Maurini, C. & Vidoli, S. (2010). Multiparameter actuation for shape control of bistable composite plates. *International Journal of Solids and Structures*, **47**, 1449–1458.

Gerson, Y., Krylov, S., Ilic, B. & Schreiber, D. (2012). Design considerations of a large-displacement multistable micro actuator with serially connected bistable elements. *Finite Elements in Analysis and Design*, **49**, 58–69.

Gigliotti, M., Wisnom, M.R. & Potter, K.D. (2004). Loss of bifurcation and multiple shapes of thin [0/90] unsymmetric composite plates subject to thermal stress. *Composites Science and Technology*, **64**, 109–128.

Golabchi, M.R. & Guest, S.D. (2009). Morphing multiscale textured shells. In *Symposium of the International Association for Shell and Spatial Structures (50th. 2009. Valencia). Evolution and Trends in Design, Analysis and Construction of Shell and Spatial Structures: Proceedings*, Editorial de la Universitat Politécnica de Valencia.

Guest, S.D. & Pellegrino, S. (2006). Analytical models for bistable cylindrical shells. *Proceedings of the Royal Society A: Mathematical, Physical and Engineering Science*, **462**, 839.

Hyer, M.W. (1981a). Calculations of the room-temperature shapes of unsymmetric laminates. *Journal of Composite Materials*, **15**, 296–310.

Hyer, M.W. (1981b). Some observations on the cured shape of thin unsymmetric laminates. *Journal of Composite Materials*, **15**, 175–194.

Lebée, A. & Sab, K. (2013). Homogenization of a space frame as a thick plate: application of the bending-gradient theory to a beam lattice. *Computers & Structures*, **127**, 88–101.

Malek, S.R. (2012). *The effect of geometry and topology on the mechanics of grid shells*. Ph.D. thesis, Massachusetts Institute of Technology.

MANSFIELD, E.H. (1962). Bending, buckling and curling of a heated thin plate. *Proceedings of the Royal Society of London. Series A, Mathematical and Physical Sciences*, **268**, 316–327.

MANSFIELD, E.H. (2005). *The bending and stretching of plates*. Cambridge University Press.

NORMAN, A.D., GOLABCHI, M.R., SEFFEN, K.A. & GUEST, S.D. (2008). Multistable textured shell structures. *Advances in Science and Technology*, **54**, 168–173.

NORMAN, A.D., SEFFEN, K.A. & GUEST, S.D. (2009). Morphing of curved corrugated shells. *International Journal of Solids and Structures*, **46**, 1624–1633.

PHAM, H.T. & WANG, D.A. (2011). A quadristable compliant mechanism with a bistable structure embedded in a surrounding beam structure. *Sensors and Actuators A: Physical*, **167**, 438–448.

PIRRERA, A., AVITABILE, D. & WEAVER, P.M. (2011). On the thermally induced bistability of composite cylindrical shells for morphing structures. *International Journal of Solids and Structures*.

RUSSELL, B., LIU, T., FLECK, N. & DESHPANDE, V. (2011). Quasi-static three-point bending of carbon fiber sandwich beams with square honeycomb cores. *Journal of Applied Mechanics*, **78**, 031008.

SALAMON, N.J. & MASTERS, C.B. (1995). Bifurcation in isotropic thinfilm/substrate plates. *International Journal of Solids and Structures*, **32**, 473–481.

SEFFEN, K.A. (2007). Morphing bistable orthotropic elliptical shallow shells. *Proceedings of the Royal Society A: Mathematical, Physical and Engineering Science*, **463**, 67.

SEFFEN, K.A. & MAURINI, C. (2013). Growth and shape control of disks by bending and extension. *Journal of the Mechanics and Physics of Solids*, **61**, 190–204.

SLOT, T. & O'DONNELL, W. (1971). Effective elastic constants for thick perforated plates with square and triangular penetration patterns. *Journal of Engineering for Industry*, **93**, 935.

TRIPATHI, D. (2002). *Practical guide to polypropylene [electronic resource]*. iSmithers Rapra Publishing.

VIDOLI, S. (2013). Discrete approximations of the föppl–von kármán shell model: From coarse to more refined models. *International Journal of Solids and Structures*, **50**, 1241–1252.

VIDOLI, S. & MAURINI, C. (2008). Tristability of thin orthotropic shells with uniform initial curvature. *Proceedings of the Royal Society A: Mathematical, Physical and Engineering Science*, **464**, 2949.

YOUNG, W.C. & BUDYNAS, R.G. (2002). *Roark's Formulas for Stress and Strain*, vol. 6. McGraw-Hill New York.
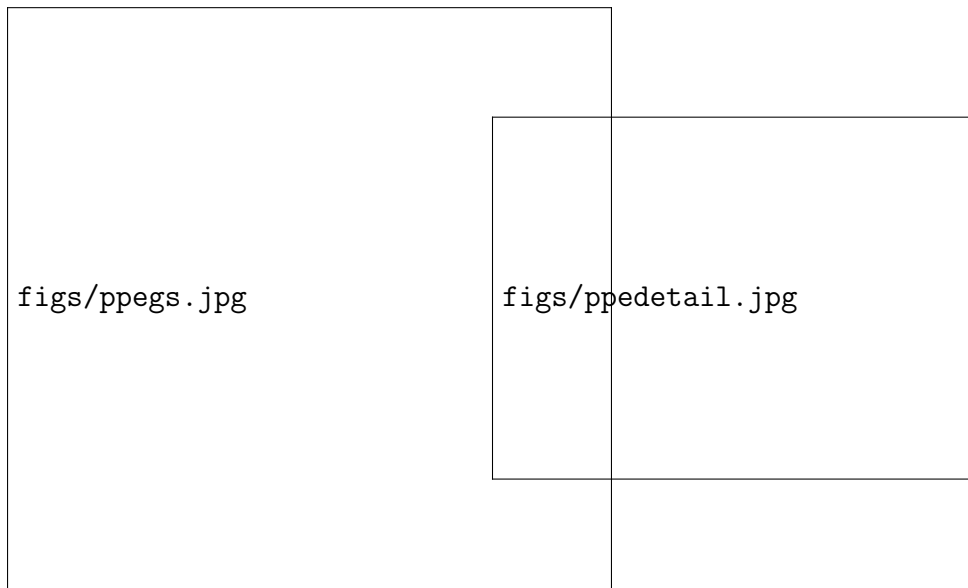
Figure 1: A honeycomb structure carved out of a solid polypropylene sheet using a water-jet cutter to produce a connected ligament network. The dimensions of the flat sheet are $300\,\text{mm} \times 300\,\text{mm}$. The unit cell has a length of $10\,\text{mm}$ while the ligament cross-section is $0.1\,\text{mm} \times 6\,\text{mm}$. The required small ligament thickness proves too delicate an operation, and results in a few imperfections, seen more clearly on the right.
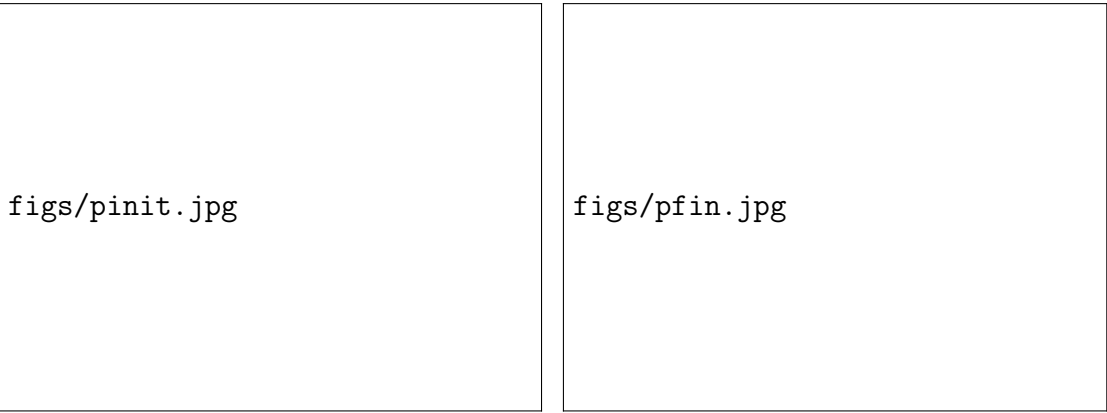
Figure 2: A polypropylene demonstrator showing the two stable geometries for a honeycomb shell design. The left image shows the initially, perfectly cylindrical geometry, while the right image shows the secondary geometry, rotated by $90°$. Although the second geometry is also approximately cylindrical, a mild curvature is also seen in the <mark>orthogonal</mark> direction. It is also clear that the radius of curvature in the second state is larger than in the initial geometry, as predicted by both the theoretical model and the FE simulations. Due to creep effects, the success of this design—with this particular material—was short-lived.

figs/deformedsin.pdf

figs/grid.pdf

figs/localgSK.jpg

figs/deformedAlign.pdf
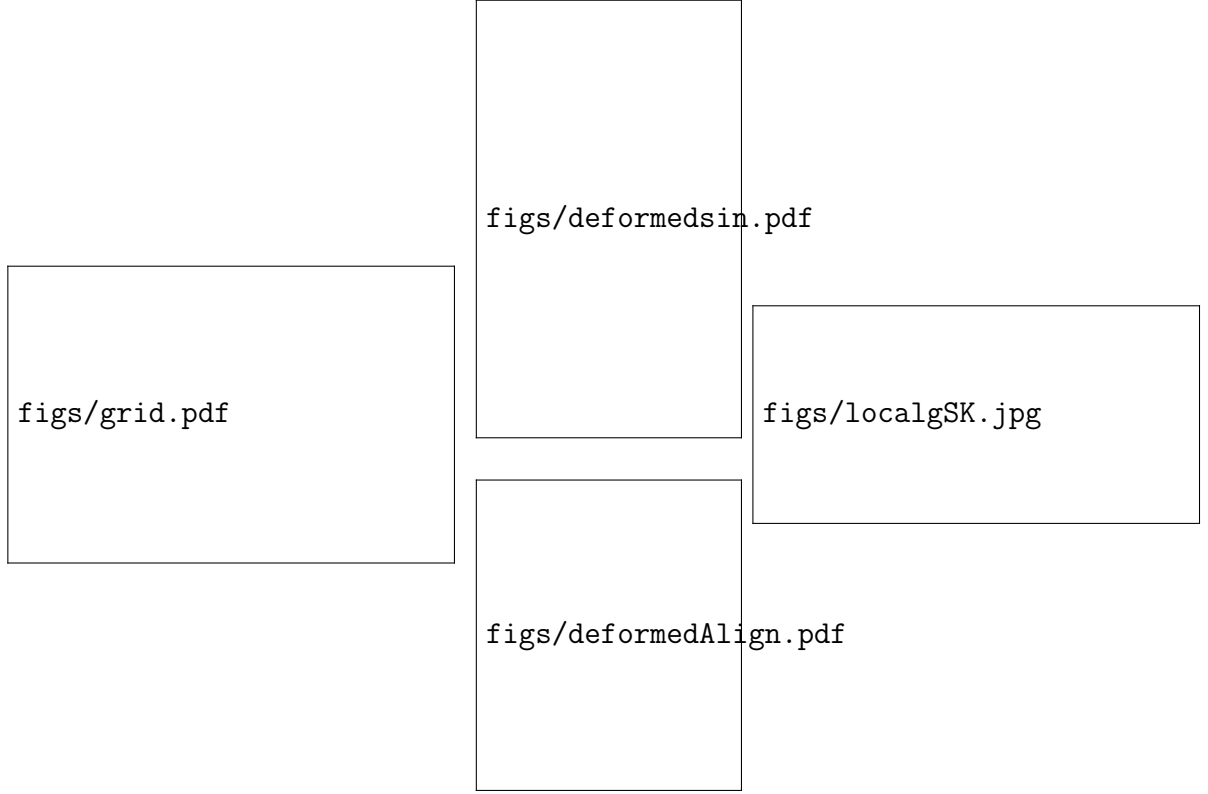
Figure 3: Detail of the square grid shell (left) and the local geometry with the relevant dimensions (right). X-Y is a fixed coordinate system in the grid shell, always aligned to the principal stiffness directions (i.e. the network); x-y is a global coordinate system that is fixed in space and is either aligned or at 45° to the X-Y system. No intermediate orientations are considered. Multistability is promoted by high Poisson's ratio and high shear modulus in the directions of the principal curvatures of the shell. Hence, we align the diagonal of the grid with these directions (x-y). A diagram of a square unit cell on a grid shell is shown in the centre, before and after the application of opposing external forces. Assuming rigid nodes, and accounting for symmetry, each beam-element is treated as an Euler-Bernoulli beam, fixed at both ends. The local (X-Y) and global (x-y) coordinate systems, are both displayed. When the two coordinate systems align, the deformation is stretching-dominated, while when they are at 45° to each other, the deformation is bending-dominated.

figs/nuagrid.pdf

figs/nudgrid.pdf
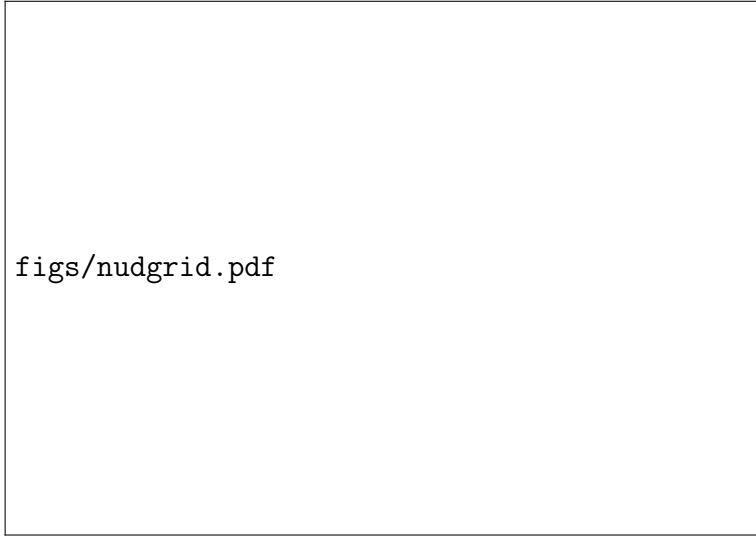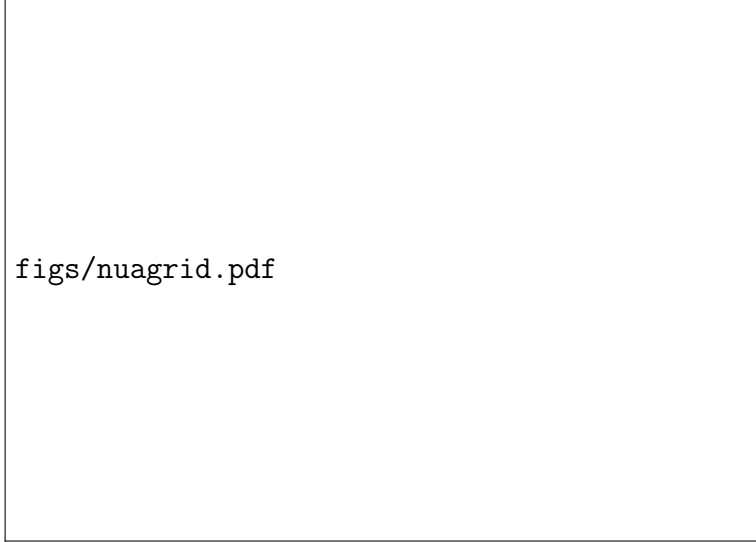
Figure 4: Plots of the variation of the Poisson's ratio and the shear modulus-related parameter for grid shell structures with respect to the local geometry. These estimates are made in correspondence to $\mathbf{A}$ and $\mathbf{D}$ matrices.

figs/globalGeom.pdf
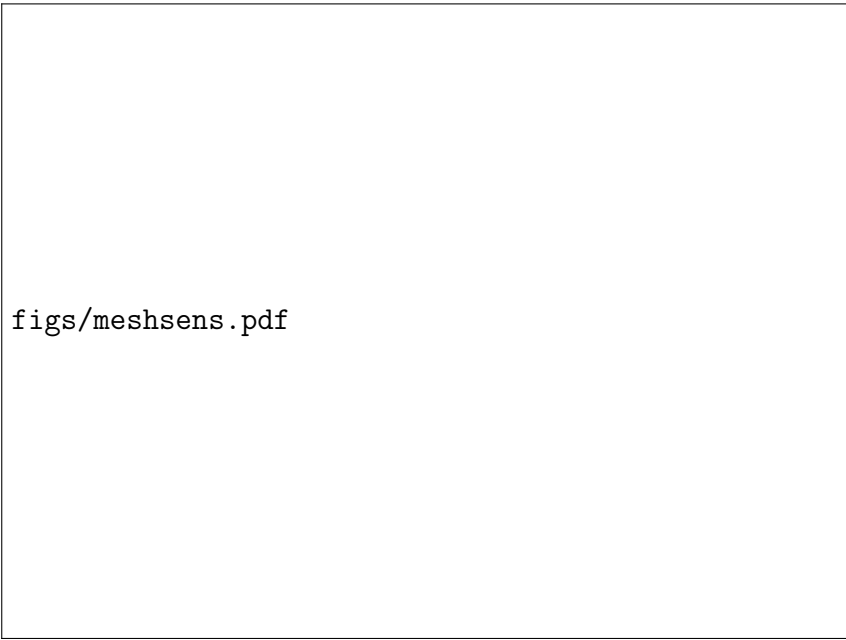
Figure 5: End view of the global initial geometry of the shell defined by the planform dimensions, a_x and a_y, and the initial curvature, ρ_x; the apex height relative to the edges is H.
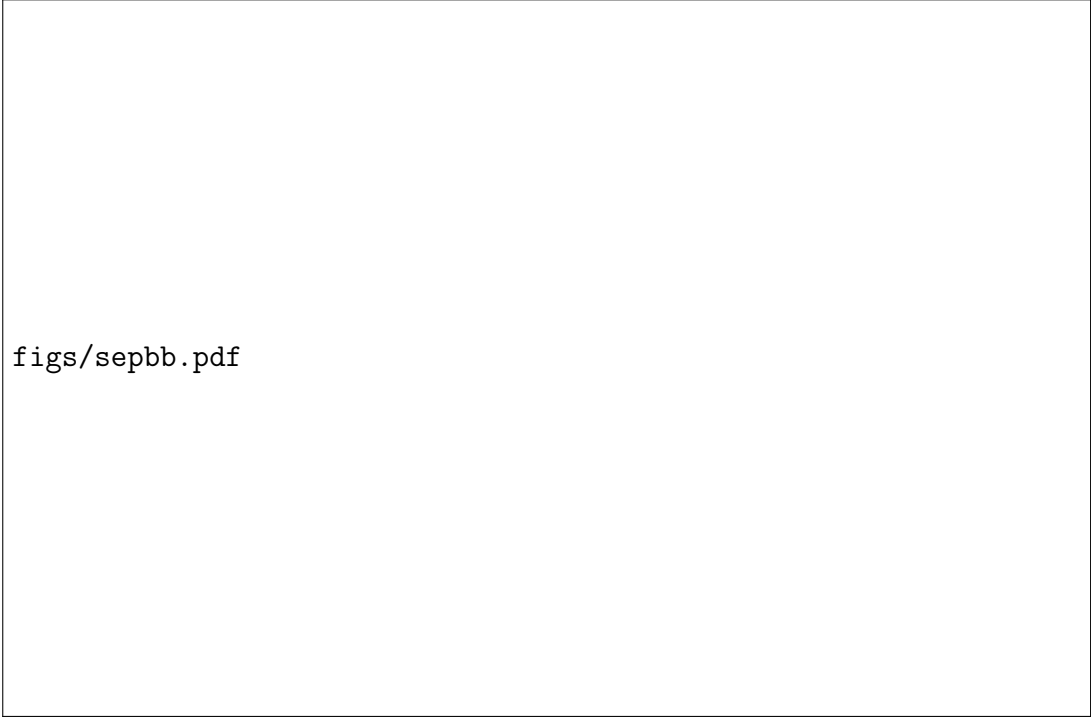
figs/grishellMid.pdf

Figure 6: In a series of finite element simulations using the commercially available software package, ABAQUS, a cylindrical grid shell is modelled with displacement control applied in the pattern indicated by arrows. The shell is free at the boundaries, but is constrained in all directions at the centre node (marked with a dot). All other nodes are completely free.
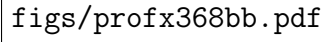
figs/meshsens.pdf

Figure 7: Different resolutions for the mesh were tested for the basic geometry of the shell, with n noting the number of elements per beam. The chosen metric is the displacement of the midpoint of one of the sides of the shell. The results are converging and four elements per beam are judged sufficient.
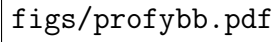
Figure 8: Strain energy for the shell, plotted against time within two Implicit Dynamic ABAQUS steps, with a duration of 100 s for each step. During the first step, the shell is gradually loaded: we can distinguish a minimum for the energy conforming to a second equilibrium geometry. In the second step, we remove the loading boundary condition and the shell returns to the second state. The value of the final strain energy is equal to the value at the minimum.

figs/profx368bb.pdf

(a) Secondary state y-profile

figs/profybb.pdf

(b) Secondary state x-profile

Figure 9: The geometry of the second state is presented here in more detail. We plot the profile of the shell for $x = 0$ and $y = 0$ respectively (the coordinate system was defined in Fig. 5). In the former case, we contrast the plot with a circular arc of 368 mm radius. The comparison shows an almost exact match. In the other perspective—shown in an exaggerated aspect ratio, curvature is more subtle. The y-profile is almost flat towards the centre, but with a more pronounced curvature towards the boundary. There is a switch in the sign of the curvature near the radial centre.
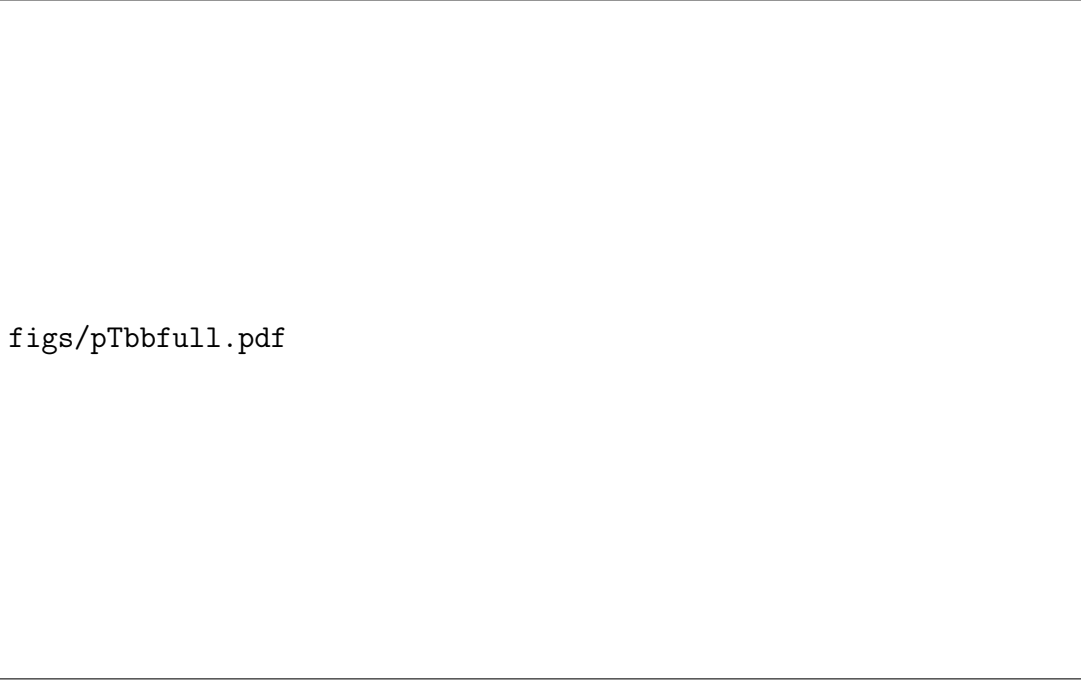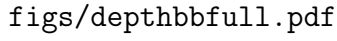
Figure 10: Comparison between force-displacement diagrams for different beam-member thicknesses. The vertical reaction force from the corner node of the shell, at which displacement control is applied, is P. Both the force and the displacement are made dimensionless by appropriate coefficients, while the beam-member width is fixed at $0.2\,\mathrm{mm}$. For a square cross-section we observe a prominent snap-through effect, but not a second equilibrium. Increasing the thickness—and hence the ratio between beam height and width—we observe a second load-free equilibrium for ratio approximately three and above. The irregularities in the plot for thinner local thickness can be attributed to local buckling effects. This induces a global rippling, detracting from the assumption of uniform deformation.
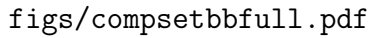
Figure 11: Results of homogenisation model for grid shell properties from Section 3.1 showing the dependence of multistability on cross-sectional dimensions. The parameter values are calculated through Eqs. (5) to (8) and then substituted into the dimensional energy expression from Eq. (9), allowing for numerical solutions for stable equilibria. We only plot values of $h > b$ in accordance with our model's assumption for Eq. (3), while the remaining variables match the values used in the FE simulations in this section. There is a cut-off point for bistability at a constant ratio between h:b, approximately equal to five.

```
figs/depthbbfull.pdf
```

Figure 12: Multistability is also affected by the initial curvature of the shell. Starting with the base grid shell case, the radius of curvature is gradually increased for a series of simulations, and dimensionless force-displacement diagrams are presented here. The last marginally bistable grid shell in this progression occurs for a radius of curvature equal to $450\,\mathrm{mm}$.
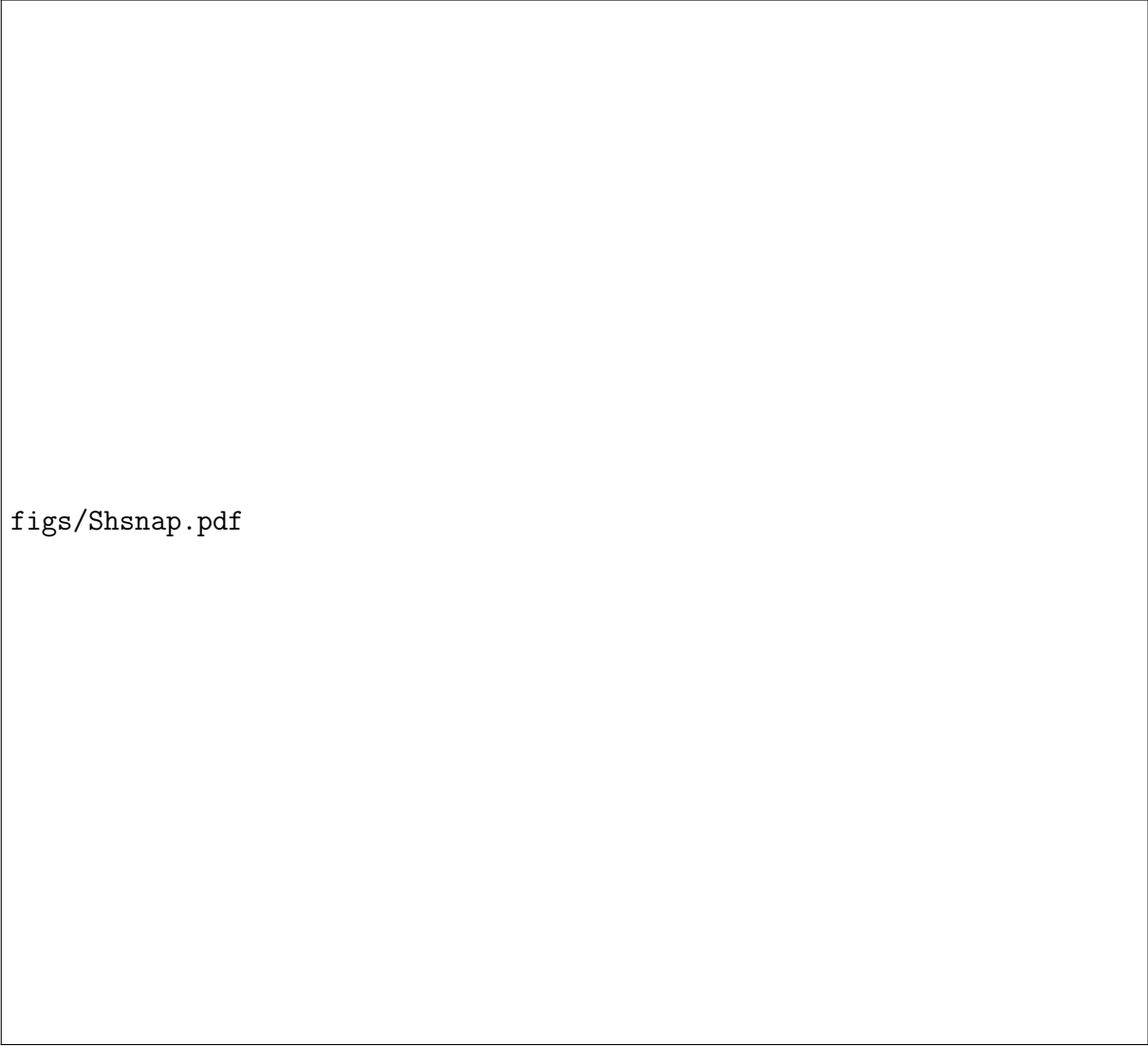
```
figs/compsetbbfull.pdf
```

Figure 13: One of the notable results of our simulations is the scaling of the energy with respect to cross-sectional dimensions of the grid shell ligaments. In this plot we compare the total strain energy for three grid shells undergoing the same displacement-controlled deformation. The three cross-sections examined are $0.02\,\mathrm{mm} \times 0.06\,\mathrm{mm}$, $0.1\,\mathrm{mm} \times 0.3\,\mathrm{mm}$ and $0.2\,\mathrm{mm} \times 0.6\,\mathrm{mm}$. The energy scales proportionally to moment of inertia of the cross-section, or hb^3, which indicates a bending-dominated deformation.

figs/hcsebb.pdf

Figure 14: Switching to a honeycomb model on ABAQUS allows for a new range of ligament geometries to be examined. An initially cylindrical shell is tested with planform dimensions $(520\,\text{mm} \times 520\,\text{mm})$, ligament length $d = 10\,\text{mm}$ and ligament thickness $b = 0.1\,\text{mm}$. By varying the ligament height, h, the upper limit of the bistable behaviour is shown to be almost $30\,\text{mm}$.

figs/Shsnap.pdf

Figure 15: The simulated transition of a honeycomb shell from an initial cylindrical geometry to a second stable configuration. The resulting shapes are similar to those for a grid shell, where the ligaments are modelled as beams. Here, the ligaments are modelled as shells and in this particular model, each ligament has dimensions $10\,\text{mm} \times 10\,\text{mm} \times 0.1\,\text{mm}$, although thicknesses up to $25\,\text{mm}$ achieved bistability for square shells of side $520\,\text{mm}$. The figure also displays the relevant thickness of the honeycomb shell compared to global dimensions. The time represents the proportional displacement actuation for the first $100\,\text{s}$ and the unloading phase for the final $100\,\text{s}$.

figs/gt.pdf
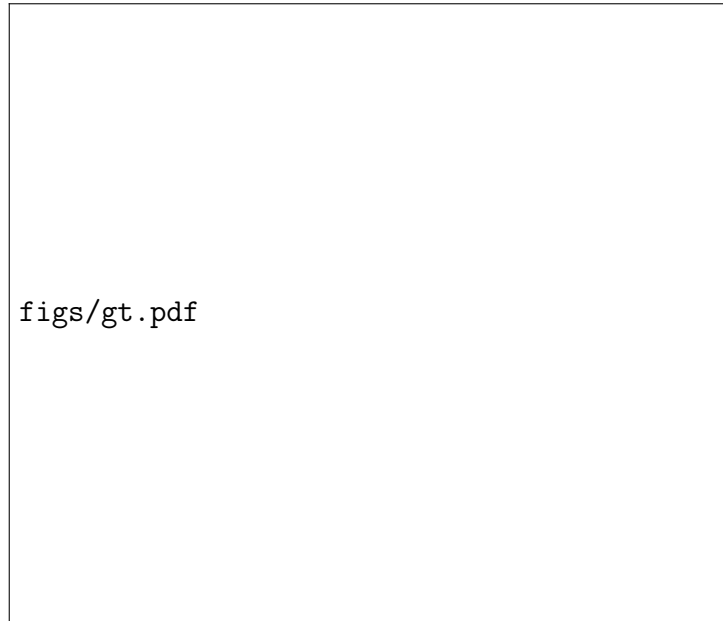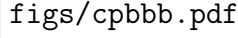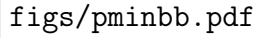
Figure 16: Comparison of the behaviour of the honeycomb structure for high values of ligament thickness—as shown in Fig. 14—with the theoretical prediction. The dimensional strain energy form of equation Eq. (9) is used to obtain the equilibria and plot the stability regions for the corresponding homogeneous shell. The global dimensions have the same values as all the simulations in this section, while for this plot the Poisson's ratio is set to a value of 0.95. Bistability is lost for values of thickness between 20–25 mm, depending on the value of the shear modulus.

(a) Strain energy contour plot

(b) Theoretical strain energy during actuation

Figure 17: The contour plot at the top shows the variation of the predicted dimensional strain energy according to Eq. (9). The global geometry is the same used throughout this section, but we assume a homogeneous shell with a Poisson's ratio of 0.95 and a shear modulus twice the isotropic value (0.5); the thickness is set at $10\,\text{mm}$. The secondary equilibrium appears at $(\kappa_x, \kappa_y) = (2.45 \times 10^{-6}, 0.00316)$ or (almost) as a same-sense cylinder with a radius of $316\,\text{mm}$—slightly larger than the initial radius. At the bottom we plot the strain energy profile along the dashed line in the top diagram. This is done for various shell thicknesses to show the correspondence to the simulated honeycomb structure results in Fig. 14.
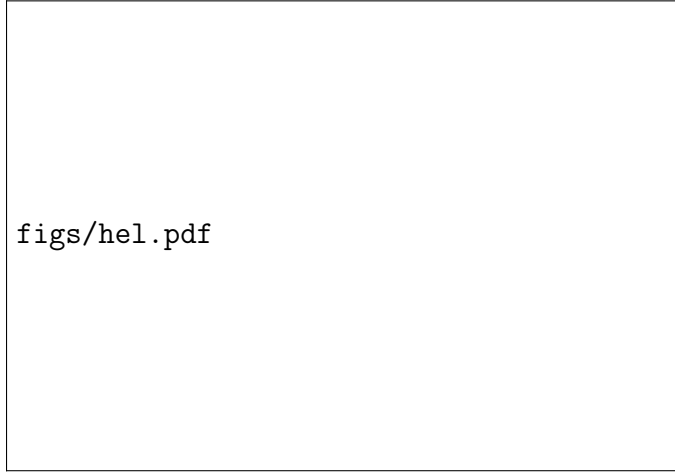
(a)
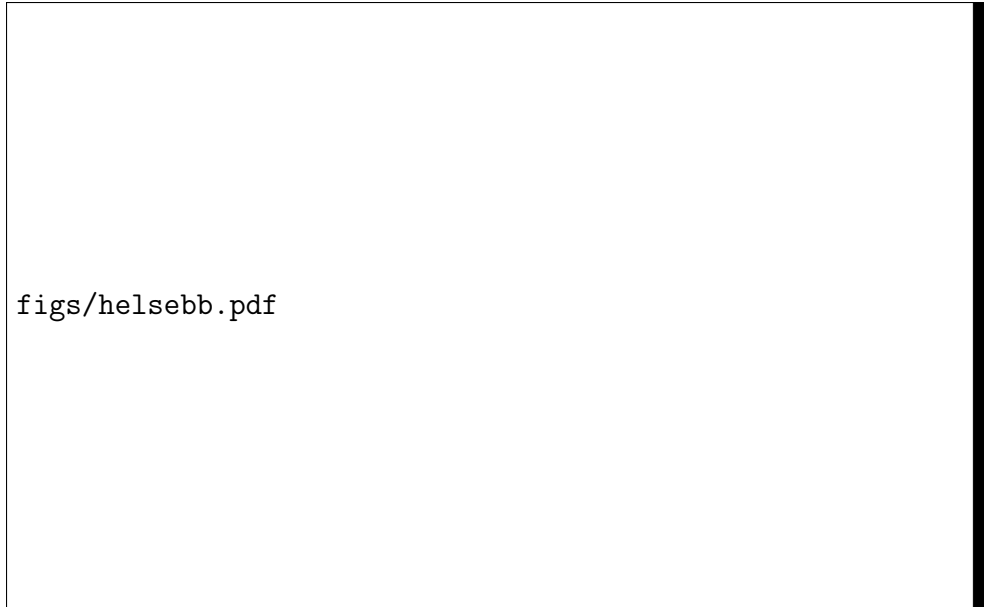
(b)

Figure 18: An initially helical, bistable grid shell is shown at the top from an ABAQUS simulation. On the left column we see the initial geometry, and on the right column the final geometry after actuation and relaxation. The top row shows a side view of the shell while the bottom row shows the shell viewed from above. At the bottom we show strain energy vs time for the helical grid shell FE simulation. We can see a clear minimum during the actuation phase (0–100 s). The actuation in this case is not optimised with respect to the second stable configuration; this might explain why the dip to the minimum is more sudden than in earlier simulations. The relaxation phase concludes at the same strain energy, confirming the bistable character of this structure.